Journal of Environmental Chemical Engineering 10 (2022) 107687

Contents lists available at ScienceDirect

Journal of Environmental Chemical Engineering

journal homepage: www.elsevier.com/locate/jece

Construction of a Fe—Cu/ceramic composite with surface electric field and far-infrared properties for effective photo-Fenton catalytic degradation of the wastewater generated from H2O2 production

Zongxian Hong, Xiunan Cai, Wuxiang Zhang, Songlin Fan, Yanjuan Zhang *, Tao Gan, Huayu Hu, Zuqiang Huang *

School of Chemistry and Chemical Engineering, Guangxi University, Nanning 530004, China

ARTICLE INFO

Keywords:
Catalytic degradation of wastewater
Photo-Fenton
Fe–Cu composite catalyst
Ceramic

ABSTRACT

To solve the complex processes for the treatment of the wastewater generated from hydrogen peroxide (H_2O_2) production and the defects of traditional Fenton reaction, a novel Fe–Cu/ceramic composite was synthesized by a combustion method and applied as a photo-Fenton catalyst for the degradation of the wastewater under visible-light irradiation. The enhancement of visible-light absorption, effective separation of electron hole pairs and stronger redox capacity of Fe–Cu/ceramic could be attributed to the surface electric field and far-infrared properties of the ceramic, thus greatly promoting its catalytic activity compared to bare Fe–Cu. Under optimized conditions (pH = 5, 50 mM of H_2O_2, and 4.0 g L^{-1} of Fe—Cu/ceramic catalyst), the COD removal rate of the wastewater achieved 96.5% within 3 h. In addition, the increased concentration of dissolved oxygen and the smaller water clusters induced by surface electric field and far-infrared ray were also beneficial for the degradation of pollutants. The excellent reusability could be attributed to the uniformly anchored bare Fe–Cu with Fe–O–Al and Cu–O–Al bonds, which reduced the leaching of metal ions. This work provides a new idea for the treatment of practical wastewater with high-efficient natural mineral-based catalysts, which possess unique performance.

1. Introduction

Hydrogen peroxide (H_2O_2) is a common eco-friendly chemical, which has been widely used in bleaching, wastewater treatment, textile industry, electronics industry, and chemical synthesis [15]. There are many methods to produce H_2O_2, including direct synthesis [14], photocatalysis [45], and anthraquinone [9]. Among them, consecutive hydrogenation and oxidation of anthraquinone are the most mature production technologies due to the advantages of low investment, high yield, and simple operation. However, a large amount of wastewater was produced in this process, including working liquid washing water, hydrogenation tower condensate, and white soil bed wastewater regeneration [27]. The wastewater mainly contains residual H_2O_2, C9–C10 arene, 2-ethyl anthraquinone, and hydroazidation degradation products. These organic compounds are insoluble in water, existing as oil in wastewater, with light orange color and strong aromatic taste [10]. The wastewater with complex chemical composition, high oxygen demand, and poor biochemical performance is difficult to be separated and degraded, which will cause great harm to the human body and the environment without efficient treatment.

At present, the methods for the disposal of the wastewater generated from H_2O_2 production include membrane treatment, biological decompression distillation, catalytic oxidation, etc. However, a single method is difficult to effectively treat the wastewater, and a combination of two or more techniques is often required. According to the characteristics of the wastewater, Fenton disposal process is usually selected for its advantages of simple operation, low operating cost, and environmental friendliness. Nevertheless, the traditional Fenton reaction has some inherent disadvantages, including narrow working pH conditions, low utilization efficiency of H_2O_2, incomplete degradation of pollutants, and the production of iron sludge [32]. Photo-Fenton method, referring to the use of light irradiation for rapid generation of highly active free radicals, can effectively improve the degradation efficiency of pollutants and overcome the defects of traditional Fenton method. Thus, it is of great feasibility and significance to develop a new photo-Fenton catalyst to treat the wastewater.

* Corresponding authors.
E-mail addresses: zhangyj@gxu.edu.cn (Y. Zhang), huangzq@gxu.edu.cn (Z. Huang).

https://doi.org/10.1016/j.jece.2022.107687
Received 15 February 2022; Received in revised form 22 March 2022; Accepted 6 April 2022
Available online 9 April 2022

Iron-based materials, a widely used photocatalyst, exhibit excellent magnetic recovery, visible-light response, and good photochemical stability [46]. However, iron-based nanoparticles exhibit low electron transfer rate, high charge recombination rate [19], and low Fe^{3+}/Fe^{2+} conversion rate [7], which greatly limit the practical application. Doping is commonly used to overcome these shortcomings [20]. It has been found that the composites exhibit stronger visible-light response, more oxygen vacancies, narrower band gaps, and faster electron transfer rates by doping Cu [5], Mn [21], or Ce [13] into iron-based materials. Among them, Cu and its oxides are narrow-bandgap semiconductors, which can absorb visible-light well. In addition, Cu^{2+}/Cu^{+} has excellent redox ability, which is similar to Fe^{3+}/Fe^{2+} [47]. Li et al. [18] found that the Cu^0 could not only promote the reduction of Fe^{3+} and Cu^{2+}, but also accelerate electron transfer between H_2O_2 and catalyst. However, bare Fe–Cu composites are easily agglomerated and leached in reaction system, leading to low catalytic activity and poor reusability. Accordingly, the loading of Fe–Cu nanoparticles on a support is one of the most common ways to solve the above problems.

Nowadays, natural minerals are applied as the supports of the nanocatalysts, and most of them have the advantages of high thermal stability and chemical stability, low cost, and good reusability [16]. Kaolin [41] and zeolite [33], widely used as the supports of Fe–Cu composites, can significantly increase the activity of the catalysts. Unfortunately, the reported functions of the supports mainly focus on improving the physical properties of dispersity and recoverability, while the composites are still suffered from the problems of high recombination rate and low electron transfer efficiency. It has been proved that the surface electric field can accelerate the separation of h^{+}/e^{-} and the concentration of carriers of semiconductors. Tourmaline, a borosilicate mineral, belonging to the trigonal space group with spontaneous polarity, far-infrared radiation, and pyroelectric properties [30]. Especially, tourmaline particles, due to the spontaneous polarity, can generate a surface electric field of 10^6–10^7 V/m [29]. Yu et al. [38] proved that the surface electric field could guide the directional transfer of photogenerated electrons to a lower the potential barrier for photo electrons or holes to readily migrate to the surface. This can realize the rapid separation of hole–electron pairs and retard their recombination, and thus increase the service life of carriers. In addition, the synergy of surface electric field and far-infrared ray can reduce the gap width, promote the ionization of water, and increase the activity of water [30]. Ceramic is prepared from a unique natural clay, and the ceramic prepared by mechanical activation [22] and bionic mineralization has similar properties (surface electric field and far-infrared radiation) to tourmaline. Therefore, in this study, the ceramic with the properties of surface electric field and far-infrared ray was used as the support of Fe–Cu bimetallic composites to prevent the aggregation of the catalysts, change the internal structure of catalysts, and activate the water in reaction system to improve catalytic efficiency for the degradation of the wastewater.

Herein, ceramic-supported Fe–Cu nanoparticles (Fe–Cu/ceramic) composite with the properties of surface electric field and far-infrared ray was synthesized and applied as a photo-Fenton catalyst to degrade the wastewater under visible-light irradiation. Different reaction conditions for the degradation of the wastewater in Fe–Cu/ceramic + H_2O_2 + Vis (visible-light) system were investigated with COD removal rate as the evaluation index, including catalyst dosage, H_2O_2 concentration, reaction time, and initial pH. Based on a series of characterizations and analyses, the effects of bare ceramics on the morphology and phase of the composites were studied, and the reasons for improving the photocatalytic performance of the composites were discussed. Finally, a potential photo-Fenton catalytic mechanism for the degradation of the wastewater was also proposed.

2. Experimental method

2.1. Materials

The wastewater generated from H_2O_2 production was supplied by Lanzhou Taibang Chemical Technology Co., LTD. (Lanzhou, China). The COD content of the wastewater was 4035 mg L^{-1}, the initial pH was 5, and the concentration of residual H_2O_2 was 0.042 mol L^{-1}. Ceramic was supplied by Kangyisheng Pottery Manufacture Co., LTD. (Qinzhou, China). Ammonium ferrous sulfate, copper acetate, potassium dichromate, sulfuric acid, silver sulfate, iron nitrate, copper nitrate, citric acid, and hydrogen peroxide were supplied by Tianjin Damao Chemical Reagent Company, China. The purity of all chemicals was analytical grade, without other purification.

The main chemical composition of the ceramic is shown in Table S1. The contents of Si, Al, Ca, Fe, and K in the ceramic were 56.7%, 17.0%, 11.3%, 5.7%, and 3.8%, respectively. The main mineral structures of the ceramic are shown in Fig. S1, indicating that the ceramic mainly contained SiO_2, Fe_2O_3, $CaAl_2Si_2O_8$, and other components. The far-infrared emissivity (8–14 μm) of the ceramic was 0.957, and the surface electric field intensity calculated by the reported method [39] was 7.932×10^7 V/m.

2.2. Preparation of Fe–Cu/ceramic composites

A combustion method was used for the synthesis of Fe–Cu/ceramic composites [6]. In a typical preparation experiment, 0.5 g of $Cu(NO_3)_2.3\ H_2O$, 0.845 g of $Fe(NO_3)_3.9\ H_2O$, and 1 g of ceramic were dissolved in 30 mL of deionized water, and then 1 g of $Cu(CH_3COO)_2.2\ H_2O$ and a certain amount of citric acid were added into the above solution and stirred for 2 h at 95 °C to form sticky gel. Then, the sticky gel was dried at 80 °C and ground into powder. Subsequently, the powder was calcined for 2 h at 400 °C in a tubular furnace under nitrogen atmosphere at a heating rate of 5 °C min^{-1}. Finally, the Fe–Cu/ceramic composite with a mass ratio of $CuFe_2O_4$:$Cu(CH_3COO)_2.2\ H_2O$:ceramic of 1:2:2 was obtained. The Fe–Cu/ceramic composites and bare Fe–Cu samples with different proportions were also prepared for comparative study in the same way.

2.3. Characterizations

The X-ray diffraction (XRD, Rigaku, Tokyo, Japan) with a Cu-Kα (λ = 0.154 nm) source was used to measure the crystal phases of different composites. The Voltage, current, and 2θ ranging were held at 40 kV, 30 mA, and 5–80°, respectively. The surface morphologies of the samples were observed using an S-3400 N scanning electron microscope (SEM, Hitachi, Japan) operated at 15 kV. The surface chemical composition and elements states were characterized by X-ray photoelectron spectroscopy (XPS) on an ESCALAB 250Xi spectrometer (Thermo Scientific, X-ray Al Kα, 1486.8 eV, USA). The surface chemical bonds were detected by Fourier transform infrared (FT-IR) spectroscopy (Thermo, USA). N_2 adsorption–desorption isotherms of the samples were determined using a nitrogen adsorption instrument (ASAP 2460). The specific surface area and pore size distribution of the samples were calculated by BET method and BJH method, respectively. The PPMS-9 vibrating sample magnetometer (VSM, Quantum Design, –20–20 kOe, USA) was used to determine the magnetism of the samples. The UV-Vis diffuse reflectance spectra of the samples were measured by a spectrophotometer (UV-3600, Shimadzu Corporation, Japan). The electron spin resonance (ESR) of the samples were measured by a A300 10/12 spectrometer (Bruck AXS Company, Germany). Electrochemical impedance spectroscopy (EIS) and cyclic voltammetry (CV) were determined by an electrochemical workstation (Princeton University Applied Research 4000 +).

2.4. Experimental procedure

Batch photo-Fenton experiments were carried out in 50 mL round-bottomed glass test tubes, and the specific operations were as follows: a certain amount of catalyst and H_2O_2 (30%) were imported into 30 mL of the wastewater, and then the mixture was transferred to photocatalytic equipment for reaction. The initial pH of the reaction solution was adjusted by HCl and NaOH. The source of visible-light was a 500 W xenon lamp (CELLB70, Beijing Zhongjiao Jinyuan Technology Co., LTD, China), with a filter that could filter ultraviolet rays below 420 nm, equipped with circulating water to keep the temperature of the outer wall chamber at 25 °C. The light intensity was 1000 W m^{-2}. The COD value of the solution at a certain time interval was determined by microwave digestion method, and the catalyst was recycled by an applied magnetic field and dried directly without any other treatment for the next cycle. All experimental results were the average of three experiments with an error of less than 5%.

3. Results and discussion

3.1. Structure and morphology characterizations

The crystalline phases of bare ceramic, bare Fe–Cu, and Fe–Cu/ceramic composites were measured by XRD analysis, as presented in Fig. 1a. The bare ceramic was mainly composed of SiO_2 and $CaAl_2Si_2O_8$ crystal phases. The diffraction peaks at $2\theta = 35.6°$ (311), 43.1° (400), 57.1° (511), and 62.7° (440) matched well with the face-centered cubic $CuFe_2O_4$ phase (JCPDS No.85–1326). The peaks at $2\theta = 43.3°$ and 50.4° corresponded to the (111) and (200) planes of face-centered cubic metallic Cu^0 (JCPDS 85–1326), revealing the good crystallinity and high purity of Fe–Cu/ceramic [2]. The diffraction peak at $2\theta = 50.4°$ and 43.1° were the characteristics of Cu^0, indicating the coexistence of $CuFe_2O_4$ and Cu^0. Noteworthy, the (400) crystal plane of $CuFe_2O_4$ in Fe–Cu/ceramic composite exhibited a slightly negative shift to lower diffraction angle, which may be ascribed to the formation of new substances by the doping of Al or other elements of the ceramic into the lattice of $CuFe_2O_4$. The results show that the bare Fe–Cu and ceramic in Fe–Cu/ceramic composite were not just a simple physical combination.

The FT-IR spectra of bare ceramic, bare Fe–Cu, and Fe–Cu/ceramic (Fig. 1b) were applied to determine the functional groups. The frequency bands at 3440 and 1620 cm^{-1} were attributed to bending O–H stretch mode and H–O–H mode. Fe–Cu/ceramic composite appeared obvious red shift at 1580 cm^{-1}, ascribed to a slight vibration of lattice oxygen caused by the formation of new bonds between Fe–Cu and ceramic. This can be conducive to the absorption of visible-light. For the bare Fe–Cu sample, the peaks at 565 and 692 cm^{-1} were related to the stretching vibration of Fe–O bond. The stretching vibration of Si–O–Si bond could be observed at 1090 cm^{-1}. In addition, the absorption intensity at 457, 795, and 1090 cm^{-1} increased, which is resulted from the increase of group polarity induced by the surface electric field of ceramic [45]. Noteworthy, the new absorption peaks at 611 and 692 cm^{-1} may be caused by the formation of metal bonds between bare Fe–Cu and bare ceramic.

Specific surface area and pore structure are two important factors affecting the activity of catalysts [17]. The N_2 adsorption–desorption isotherms and pore size distribution plots of bare Fe–Cu, ceramic, and Fe–Cu/ceramic are displayed in Fig. 1c, and the corresponding parameters are presented in Table S2. The isotherms of all samples were type III adsorption branch with a type H3 hysteresis loop, revealing the mesoporous structure [24]. This indicates that the samples presented multilayer adsorption [1], which was consistent with the SEM result. Compared to ceramic and bare Fe–Cu, the Fe–Cu/ceramic composite exhibited the highest specific surface area (19.2 m^2 g^{-1}), largest pore volume (0.106 cm^3 g^{-1}), and smallest average pore diameter (20.6 nm).

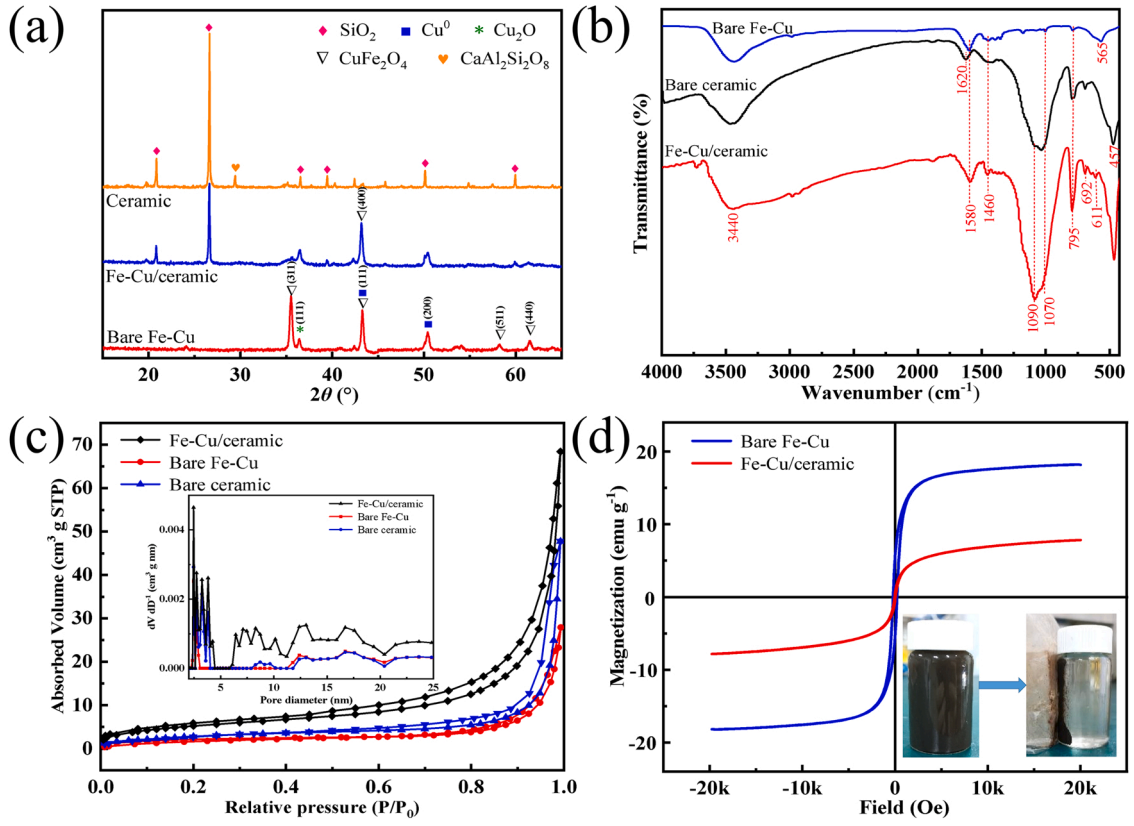

Fig. 1. (a) XRD patterns, (b) FT-IR spectra, and (c) N_2 adsorption–desorption isotherms and pore size distribution plots of bare ceramic, bare Fe–Cu, and Fe–Cu/ceramic; (d) magnetic hysteresis curves of bare Fe–Cu and Fe–Cu/ceramic (inset shows the separation of Fe–Cu/ceramic composite from the solution by a magnet).

The improvement of specific surface area could be attributed to the uniform dispersion of Fe–Cu nanoparticles and the increase of pore volume in ceramic, while the increase of pore volume was due to the accumulation of ceramic pieces and the pores formed by the pyrolysis of sol-gel. The high specific surface area and favorable pore structure will be beneficial for the migration and degradation of target pollutants [36].

Magnetic properties are significant for the recycle of the catalyst [42]. Fig. 1d shows the magnetic hysteresis of bare Fe–Cu and Fe–Cu/ceramic composite at room temperature under an applied magnetic field of 2 T. The saturation magnetization (Ms) of bare Fe–Cu was 18.2 emu g^{-1}. After introducing non-magnetic ceramics, the Ms of the Fe–Cu/ceramic composite decreased to 7.83 emu g^{-1}. The residual magnetization (0.186 emu g^{-1}) and coercivity (0.0200 Oe) of Fe–Cu/ceramic composite were not obvious, indicating that

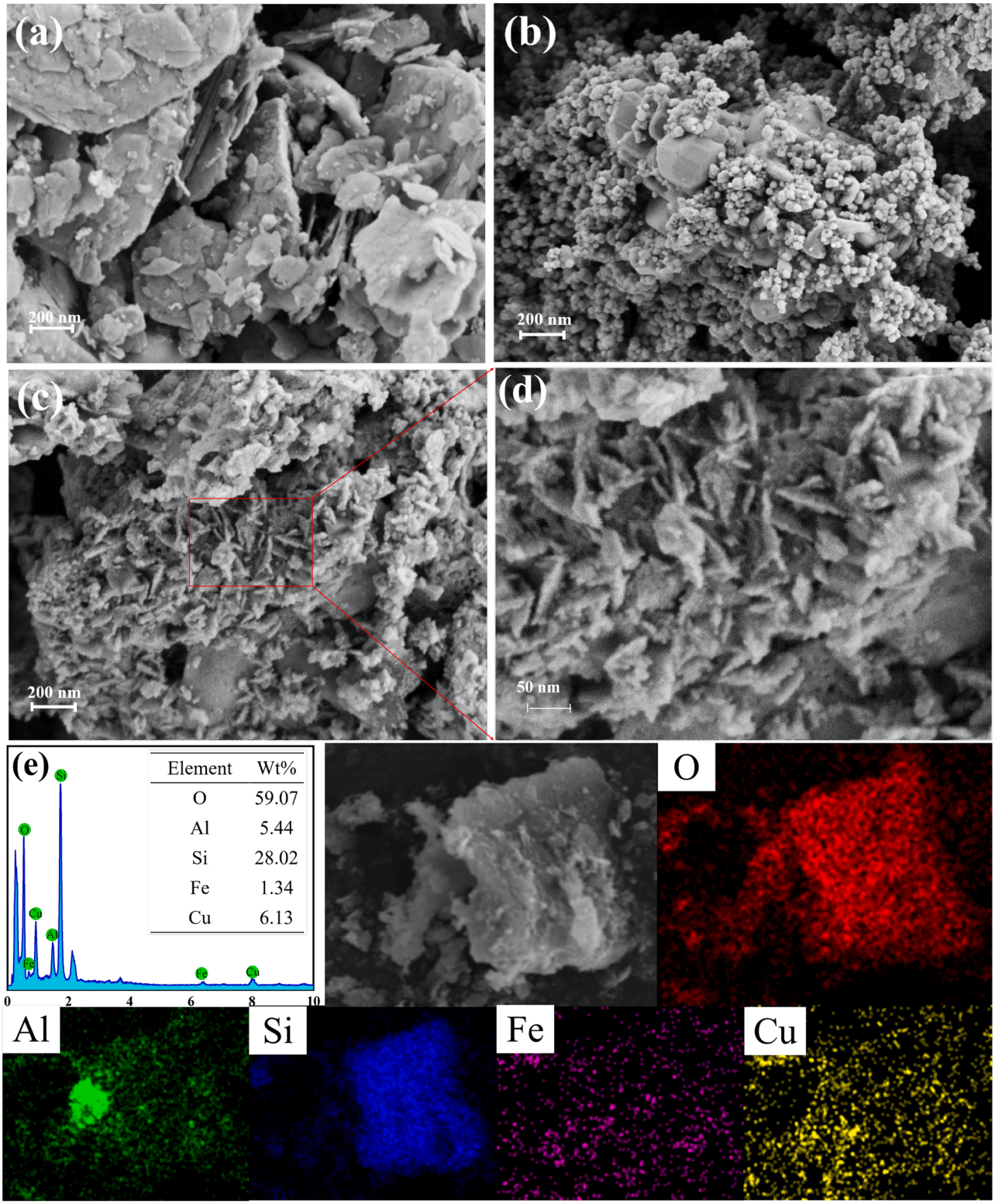

Fig. 2. SEM images of (a) bare ceramic, (b) bare Fe–Cu, and (c, d) Fe–Cu/ceramic composite; (e) EDX and element (O, Al, Si, Fe, and Cu) mappings of Fe-Cu/ceramic.

Fe–Cu/ceramic composite had superparamagnetism, which is conducive to the separation and treatment of catalyst from the reaction system.

The morphologies of bare ceramic, bare Fe–Cu, and Fe–Cu/ceramic were observed by SEM. As shown in Fig. 2a, the bare ceramic was comprised of smoothly stacking sheet. The smooth layer was parallel with single crystal, which is favorable to the uniform dispersion and loading of Fe–Cu nanoparticles. The bare Fe–Cu nanoparticles exhibited serious agglomeration, distributing with tightly packed spherules on the surface (Fig. 2b). As the loading of Fe–Cu nanoparticles on the ceramic, the auricular-shaped and petal-like nanosheets were spatially interconnected and vertically grew on the surface of the ceramic, thus exposing abundant edges and sharp corners (Fig. 2c). The decrease in the size of Fe–Cu particles is related to the regulation of surface electric field [23]. The unique morphology of Fe–Cu/ceramic can provide abundant active sites for rapid electron transfer between the catalyst and H_2O_2. Moreover, this is also beneficial to the reflection of light and the increase in residence time and utilization rate, resulting in the improvement of photocatalytic efficiency. The element mapping images (Fig. 2e) clearly revealed the uniform distribution of O, Al, Si, Fe, and Cu species in the Fe-Cu/ceramic. Additionally, the atomic contents of O, Al, Si, Fe, and Cu species were 59.07%, 5.44%, 28.02%, 1.34%, and 6.13%, respectively.

3.2. Surface element composition analysis

The surface element composition of Fe–Cu/ceramic and bare Fe–Cu were elucidated by XPS analysis. Six elements (C, O, Fe, Cu, Al, and Si) of the Fe–Cu/ceramic composite could be observed in the full-scan XPS spectrum (Fig. 3a). The O 1s spectrum (Fig. 3b) of Fe–Cu/ceramic could be fitted to 533.7, 531.9, 530.9, and 529.3 eV, corresponding to O–H,

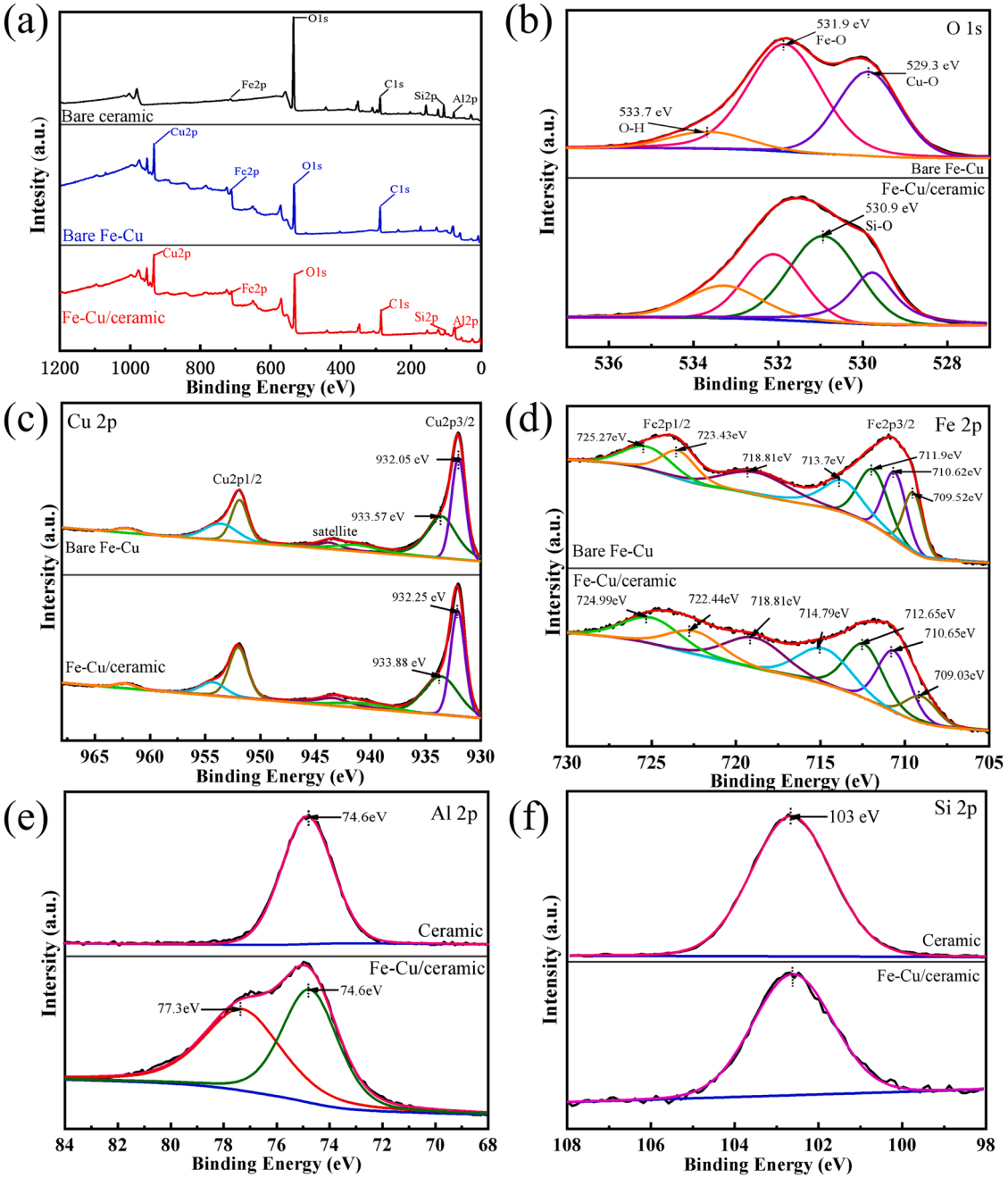

Fig. 3. XPS spectra of (a) survey, (b) O 1 s, (c) Cu 2p, (d) Fe 2p, (e) Al 2p, and (f) Si 2p for bare Fe–Cu and Fe–Cu/ceramic.

Si–O, Fe–O, and Cu–O, respectively [3]. Compared with bare Fe–Cu, the increased strength of hydroxyl peak of the composite was attributed to the introduction of ceramic with rich hydroxyl groups. The increase of surface hydroxyl groups could enhance the mass transfer between the catalyst and pollutants and efficiently activate H_2O_2 to produce more reactive radicals [6]. In Cu 2p spectrum (Fig. 3c), the peaks at 932.72 and 934.29 eV were ascribed to Cu^0 and Cu^{2+}, respectively, further confirming the coexistence of Cu^{2+} and Cu^0 in Fe–Cu/ceramic [5].

For Fe 2p spectrum (Fig. 3d), Fe $2p_{3/2}$ could be divided into four different peaks. Among them, the peaks at 710.62 and 711.9 eV corresponded to Fe^{3+} octahedral species and Fe^{3+} tetrahedron species, and those at 709.52 and 713.7 eV corresponded to Fe^{2+} octahedral species and the high spin Fe^{2+} [11]. Noteworthy, the Cu 2p and Fe 2p peaks in Fe–Cu/ceramic composite showed a positive shift, which may be caused by the new chemical bonding between Fe–Cu and ceramic. To further compare the chemical coordination between ceramic and Fe–Cu in Fe–Cu/ceramic, the Al 2p and Si 2p spectra of Fe–Cu/ceramic and bare Fe–Cu were investigated [40]. As shown in Fig. 3e, a new peak appeared at 77.3 eV in Al 2p spectrum of Fe–Cu/ceramic, while almost no difference in Si 2p spectrum (Fig. 3f), suggesting that the formation of Fe–O–Al and Cu–O–Al bonds between Fe–Cu and ceramic [6]. The XPS result demonstrates that Fe–Cu and ceramic were bound by chemical bond, which was conducive to reduce metal leaching and increase the reusability of Fe–Cu/ceramic composite.

3.3. UV–vis diffuse reflection spectrum and electrochemical characterization

The optical absorption properties of different samples were studied by UV–Vis diffuse reflectance spectrum (DRS). As shown in Fig. 4a, the bare ceramic exhibited low light absorption in the full wavelength range, which was related to its diffuse reflection [6]. Compared with bare Fe–Cu, the absorbance intensity of Fe–Cu/ceramic presented a significant enhancement in the visible-light region range, and the highest absorption point showed a redshift from 480 to 582 nm. The enhancement of absorption intensity is ascribed to that the unique auricula-like structure of the composite increased the light reflection and made full use the light source. The redshift of absorption edge is due to that the ceramic with surface electric field could induce electron polarization and reduce the gap [44]. Moreover, the bandgap of the samples was calculated by using Kubelka-Munk function. The bandgap of Fe–Cu/ceramic was about 1.31 eV, lower than that of bare Fe–Cu (1.61 eV), indicating that Fe–Cu/ceramic could generate more intermediate energy levels and more active species per unit time [12]. Therefore, the Fe–Cu/ceramic catalyst showed wider and better absorption in the visible-light region, attributed to the synergistic effect of Fe–Cu and ceramic, thus improving the photocatalytic activity.

The electron transfer ability and Fe^{3+}/Fe^{2+} redox ability of bare ceramic, bare Fe–Cu, and Fe–Cu/ceramic were explored by EIS spectra and CV curves, and the results are shown in Fig. 4. Smaller arc radius in EIS map means the smaller interfacial charge transfer resistance and higher conductivity [28]. As shown in Fig. 4b, the Rct values of Fe–Cu/ceramic, bare Fe–Cu, and bare ceramic were 160, 346, and 754 Ω, respectively. Fe–Cu/ceramic had the smallest semi arc, indicating that the introduction of ceramic contributed to better charge transfer. The electrons generated by Fe–Cu active sites were rapidly transferred to the catalyst surface credited to the surface electric field of ceramic under visible-light irradiation, which could effectively promote the separation and transmission of electron holes, thus improving the photocurrent response. Fig. 4c shows that the *I*pa (oxidation peak currents) and *E*pa (potential) of bare Fe–Cu were 140.3 μA and 0.253 V, respectively, and had the largest potential difference ($\Delta Ep = 0.206$ V). However, the oxidation peak value increased significantly, and the reduction potential decreased by 0.042 V after the introduction of ceramic. Δ*E*p decreased to 0.168 V, indicating that the highest redox ability of Fe^{3+}/Fe^{2+} in Fe–Cu/ceramic. Consequently, the introduction of ceramic could effectively shorten the electron transfer distance, thus increasing the reversibility of the Fe–Cu/ceramic catalyst.

3.4. Photo-Fenton catalytic degradation performance for treating the wastewater

3.4.1. Determination of optimum proportion

The COD removal rates of the wastewater catalyzed by the Fe–Cu/ceramic composites with different proportions ($CuFe_2O_4$:Cu $(CH_3COO)_2$.2 H_2O:ceramic) were investigated. As shown in Fig. 5a, the Fe–Cu/ceramic composite with the mass ratio of 1:2:2 exhibited the excellent COD removal rate (91.3%), higher than those with the ratio of 1:1:1 (86.6%) and 1:5:5 (85.7%). The COD removal rate showed a trend of rising first and then falling with the increase of the $CuFe_2O_4$ loading ratio, which could be attributed to the agglomeration of Fe–Cu active components, leading to the decrease of active sites and adsorption capacity. Furthermore, the COD removal rate data of the wastewater catalyzed by different catalysts were fitted by pseudo-first order kinetic model, and the reaction rate constant (*k*) values were calculated. As shown in Table S3, the *k* value of Fe–Cu/ceramic (1:2:2) + H_2O_2 + Vis system was 0.1675 h^{-1}, which was fitted well with the pseudo-first order kinetic model. Fig. 5b presents the degradation of the wastewater in different systems. The adsorption of catalyst played a major role without light source. The degradation efficiency of the wastewater in Fe–Cu/ceramic (1:2:2) + H_2O_2 + Vis system was 91.3%, much higher than other systems.

The size of water clusters is usually expressed by the half peak width of ^{17}O NMR, and the smaller half peak width indicates the smaller water clusters [35]. The smaller water cluster implies the higher activity, which is more favorable for the photocatalytic reaction. As presented in Fig. 5d and e, the half peak width of ^{17}O NMR changed from 70.83 to 47.49 Hz after treated with Fe–Cu/ceramic composite, indicating the reduction in the size of water clusters in the reaction system. Moreover, the concentration of dissolved oxygen in pure water increased from 3.33

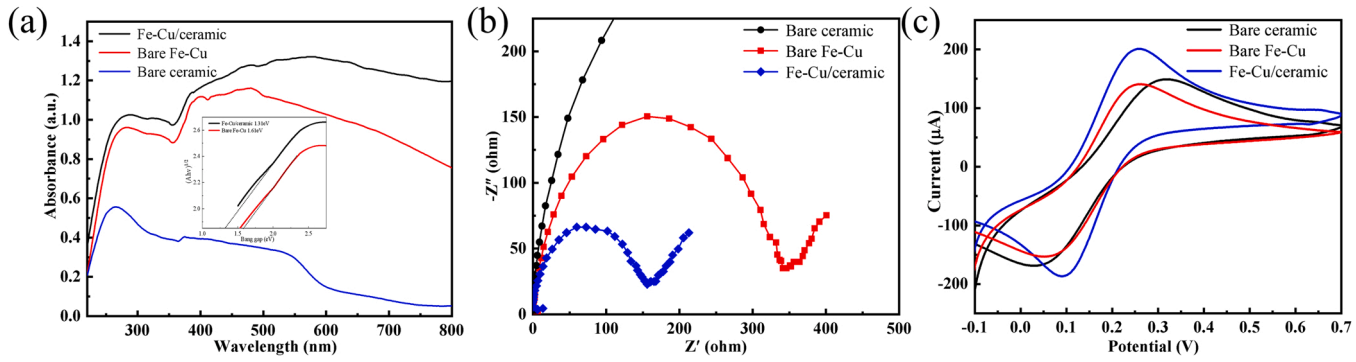

Fig. 4. (a) UV–vis DRS (inset: band gaps), (b) EIS spectra, and (c) CV curves of bare ceramic, bare Fe–Cu, and Fe–Cu/ceramic.

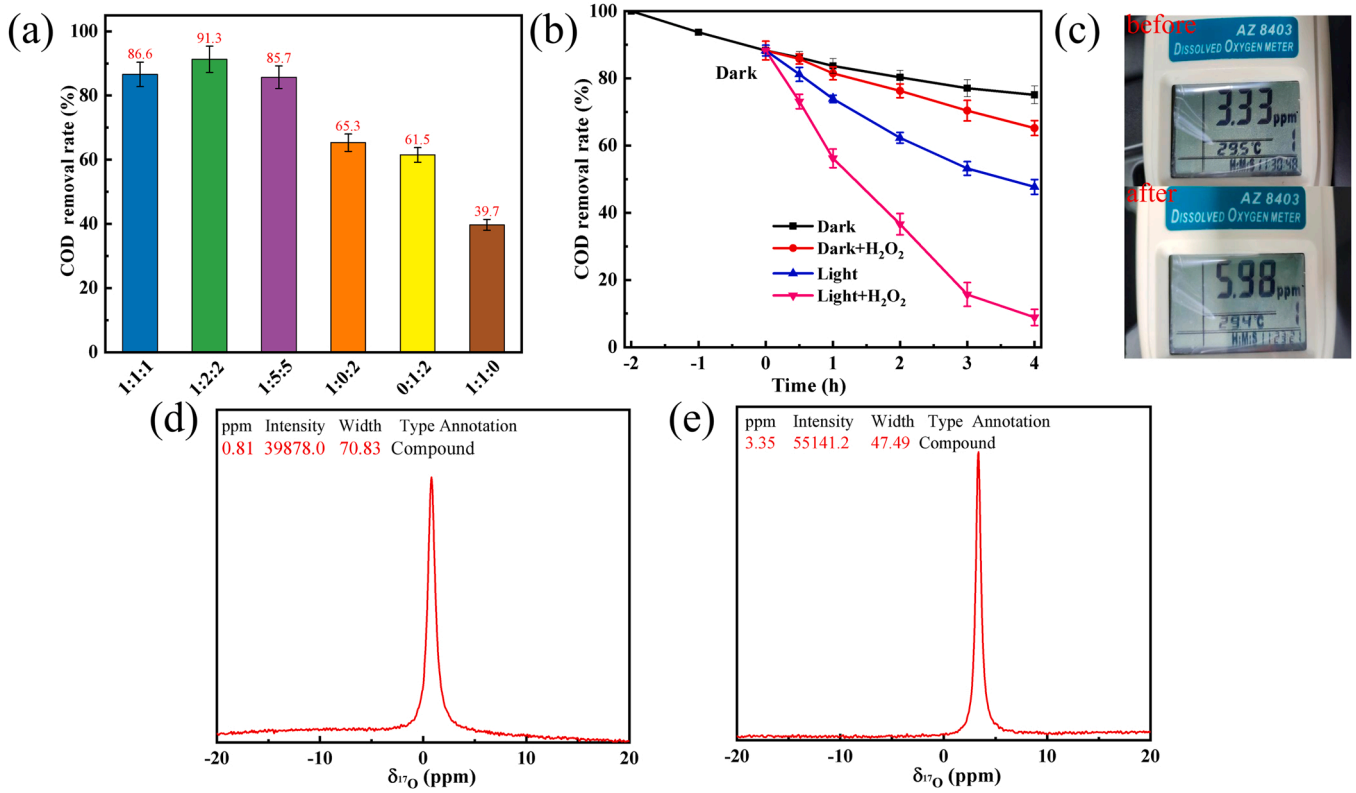

Fig. 5. (a) COD removal rates of the wastewater catalyzed by the Fe–Cu/ceramic composites with different proportions, (b) the degradation of the wastewater in different systems, (c) the concentration of dissolved oxygen in pure and treated water, and the changes in the half peak width of ^{17}O NMR of water cluster (d) before and (e) after the reaction.

to 5.98 mg L^{-1} after treated with Fe–Cu/ceramic for 3 h (Fig. 5c). As a result, the Fe–Cu/ceramic composite with a ratio of 1:2:2 exhibited good catalytic activity in H_2O_2 activation. It may be explained as following cases: (1) the introduction of ceramic increased the specific surface area and pore volume of the composites, providing more active sites; (2) the rich surface hydroxyl of ceramic could not only promote the decomposition of H_2O_2, but also enhance the mass transfer between pollutants and catalyst; (3) the surface electric field and far-infrared properties of the ceramic could reduce the size of water clusters, contributing to high diffusion force, activity, and oxygen content, which are conducive to the migration of target pollutants and the generation of superoxide radicals [37].

3.4.2. *Effect of reaction conditions on COD removal rate*

The degradation rate is closely related to the catalyst dosage. As shown in Fig. 6a, when the amount of catalyst increased from 0.5 to 4 g L^{-1}, the COD removal rate of the wastewater increased from 47.7% to 94.4%. However, when the catalyst dosage continued to increase, the COD removal rate was slightly improved, ascribed to that there were already enough catalytic sites and excessive catalyst might capture and consume active free radicals. Therefore, the catalyst dosage for subsequent photo-Fenton experiments were selected as 4 g L^{-1}.

The degradation of the wastewater with different H_2O_2 concentrations was studied. The result (Fig. 6b) shows that the COD removal rate of the wastewater increased rapidly from 43.7% to 94.4% with increasing H_2O_2 from 0 to 50 mM. However, the degradation rate did not increase when H_2O_2 concentration increased from 50 to 200 mM, which may result from the scavenging of radical·OH by excessive H_2O_2 [31] (Eqs. (1) and (2)).

$$OH + H_2O_2 \rightarrow \cdot OOH + H_2O \quad (1)$$

$$OH + \cdot OOH \rightarrow H_2O + O_2 \quad (2)$$

The influences of reaction time and initial pH on COD removal rate are shown in Fig. 6c and d. Obviously, the COD removal rate increased with the extension of reaction time, ascribed to that the more active species were generated. The high degradation rate resulted in efficient degradation of more pollutants. The initial pH affects the surface potential of the catalyst and the leaching of metal ions. Fig. 6d shows that the COD removal rate decreased with the increase of initial pH, and the COD removal rate was the highest when the pH was 2–3.5. This is because Fe^{2+} and Cu^{+} were easy to leach from the catalyst into the solution under strong acid conditions, thus accelerated the decomposition of H_2O_2. Under alkaline conditions, H_2O_2 was easy to be decomposed as H_2O and O_2, and the Fe^{3+} and Cu^{2+} could easily precipitate with excessive hydroxide (OH^-) [4]. It is worth noting that Fe–Cu/ceramic catalyst exhibited good catalytic activity in the pH range of 2–9.5, which could avoid the adjustment of pH and was conducive to the repeated use of the catalyst, realizing great significance for its practical application.

In general, the existing positive and negative ions of the actual wastewater have positive or negative effects on the degradation effect. The effect of typical ions (such as Mg^{2+}, Ca^{2+}, Na^{+}, Cl^{-}, SO_4^{2-}, HCO_3^{-}, NO_3^{-}) on COD removal rate of the wastewater was studied under optimized conditions (Fig. S2). The Mg^{2+} and Ca^{2+} displayed strong inhibition in Fe-Cu/ceramic + H_2O_2 + Vis system, with COD removal rate decreasing from 96.5% to 85.6% and 80.5%, respectively, which could be attributed to the ionic strength effect of high valence cations [34]. There was no significant impact of the addition of Na^{+} and NO_3^{-} on the degradation of the wastewater [6]. The presence of Cl^{-} and SO_4^{2-} improved the degradation efficiency of the wastewater, which could be attributed to the formation of Cl· and $SO_4^{\cdot -}$ free radicals [8]. In addition, the negative effect of HCO_3^{-} on the degradation of the wastewater was related to that the active sites of the catalyst were occupied and the·OH radicals were quenched [25].

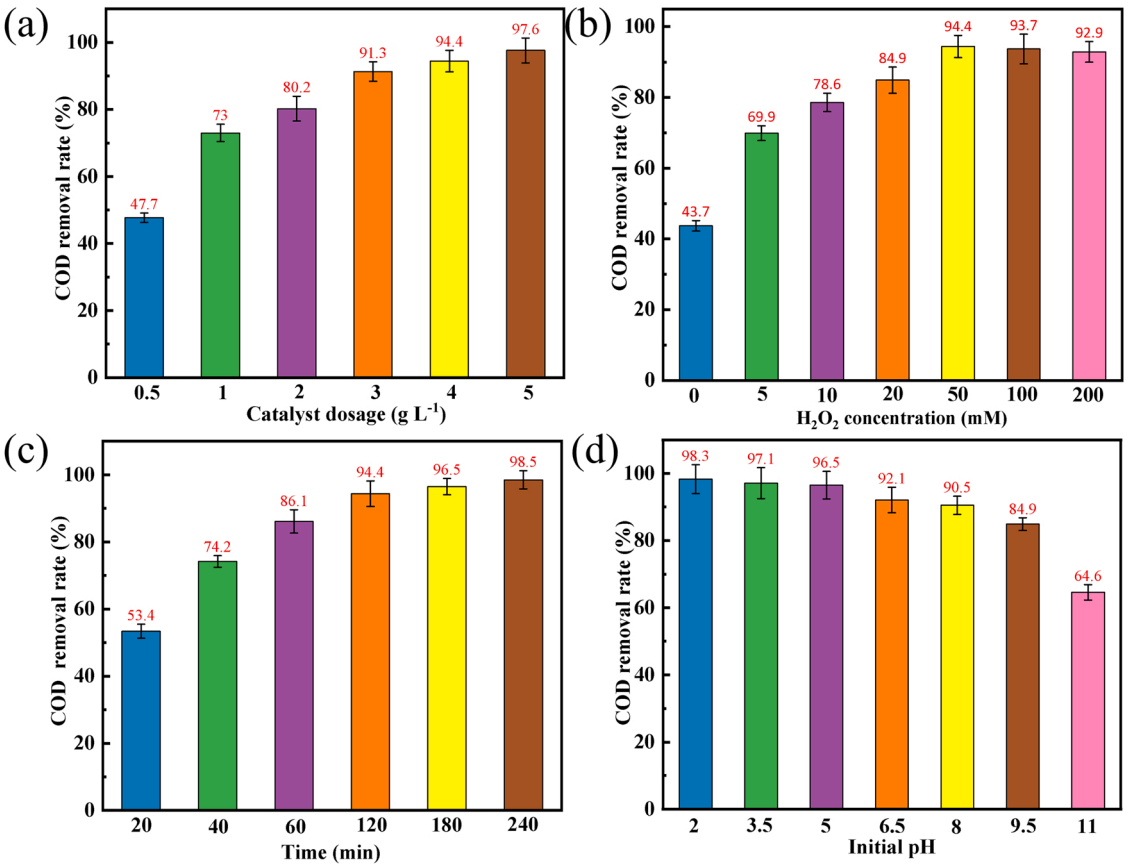

Fig. 6. Effects of (a) catalyst dosage, (b) H_2O_2 concentration, (c) reaction time, and (d) initial pH on the COD removal rate with Fe–Cu/ceramic as catalyst. Experimental conditions: T = 25 °C; catalyst dose = 4 g L^{-1} (expect a); H_2O_2 concentration = 50 mM (expect b); reaction time = 3 h (expect c); pH = 5.0 (expect d).

3.5. Stability and reusability of the Fe–Cu/ceramic catalyst

The stability and reusability of the Fe–Cu/ceramic catalyst are essential for its practical application. As can be seen from Fig. 7a, the Fe–Cu/ceramic catalyst showed high stability with COD removal rate of 84.2% after successive use of 5 times. The fresh and used Fe–Cu/ceramic catalysts were characterized by FTIR (Fig. 7d). The FTIR spectra of used catalysts showed no obvious change compared with that of the fresh catalyst, indicating that the catalyst was relatively stable. In addition, the new absorption peak at 2900 cm^{-1} corresponded to undegraded pollutants. To further identify the stability of the catalyst, the leaching concentrations of Fe and Cu after each cycle were monitored by an atomic flame method (Fig. 7b and c). The highest Cu leaching concentration (5.87 mg L^{-1}, making up 0.57% of total Cu amount in Fe–Cu/ceramic) of Fe–Cu/ceramic was much lower than that of bare Fe–Cu (61.6 mg L^{-1}, making up 5.98% of total Cu amount in Fe–Cu). In addition, the maximum Fe leaching concentration was 0.91 mg L^{-1}, which is lower than the United States and the European Union discharge standards (2 mg L^{-1}) [18]. The element mapping images of the Fe–Cu/ceramic catalyst after cycle tests had no significant difference in atomic content, further indicating the stability of the catalyst (Fig. S3). In addition, a slight decrease in the Cu content could be attributed to ion leaching. The relatively lower Fe leaching might be attributed to the generation of Fe–O–Al and Cu–O–Al bonds between Fe–Cu and ceramic. This phenomenon is well consistent with the XPS result.

3.6. Identification of the dominant radicals

To reveal the catalytic mechanism for the degradation of the wastewater over Fe–Cu/ceramic under visible-light irradiation, different types of radical scavengers were used to detect the active substances in the photo-Fenton reaction system. As shown in Fig. 8b, the activities of·OH,·O_2^-, e^-, and h^+ generated from photo-Fenton catalytic reaction were illuminated by the addition of 10.0 mM scavengers (IPA, BQ, EtOH, and KI) in the reaction system, respectively. When IPA and BQ were added, the COD removal rate significantly decreased from 96.5% to 23.1% and 75.6%, respectively. By contrast, the addition of KI and EtOH led to a slight decrease of COD removal rate, revealing that·OH and·O_2^- were the main reaction species in the photo-Fenton system. The characteristic spectra of DMPO-·OH and DMPO-·O_2^- were also identified in the reaction system after 10 min of irradiation. As shown in Fig. 8a, DMOPO-·O_2^- signals with a strength ratio of 1:2:2:1 and DMOPO-·O_2^- signals with a strength ratio of 1:1:1:1 could be observed, which further prove that·OH and·O_2^- were generated in the reaction system [43]. Therefore, the·OH and·O_2^- were the main reactive species, and the·OH was mainly formed by the decomposition of H_2O_2, while·O_2^- was mainly formed by capturing photogenerated electrons by dissolved oxygen that increased by surface electric field and far-infrared ray.

3.7. Possible photo-Fenton reaction mechanism

The XPS analysis of fresh and used Fe–Cu/ceramic catalysts was applied to further determine the reactive sites, and the results are presented in Fig. 9. The full-scan XPS spectrum of used Fe-Cu/ceramic had no significant change compared with that of fresh catalyst, indicating that the catalyst was relatively stable (Fig. 9a). In the Cu 2p spectra, the peak area ratio of Cu^{2+} increased from 47.4% to 56.1% (Fig. 9c), indicating the transition of Cu^0 to Cu^{2+} because of the erosion of Cu^0 in the photo-Fenton reaction. As shown in Fig. 9d, the peak area ratio of Fe^{2+} increased from 14.9% to 24.1%, indicating that more Fe^{2+} facilitated the decomposition of H_2O_2 to produce more·OH. The increased ratio of Fe^{2+} is due to the reduction of Fe^{3+} to Fe^{2+} by the Cu^+ formed from Cu^0

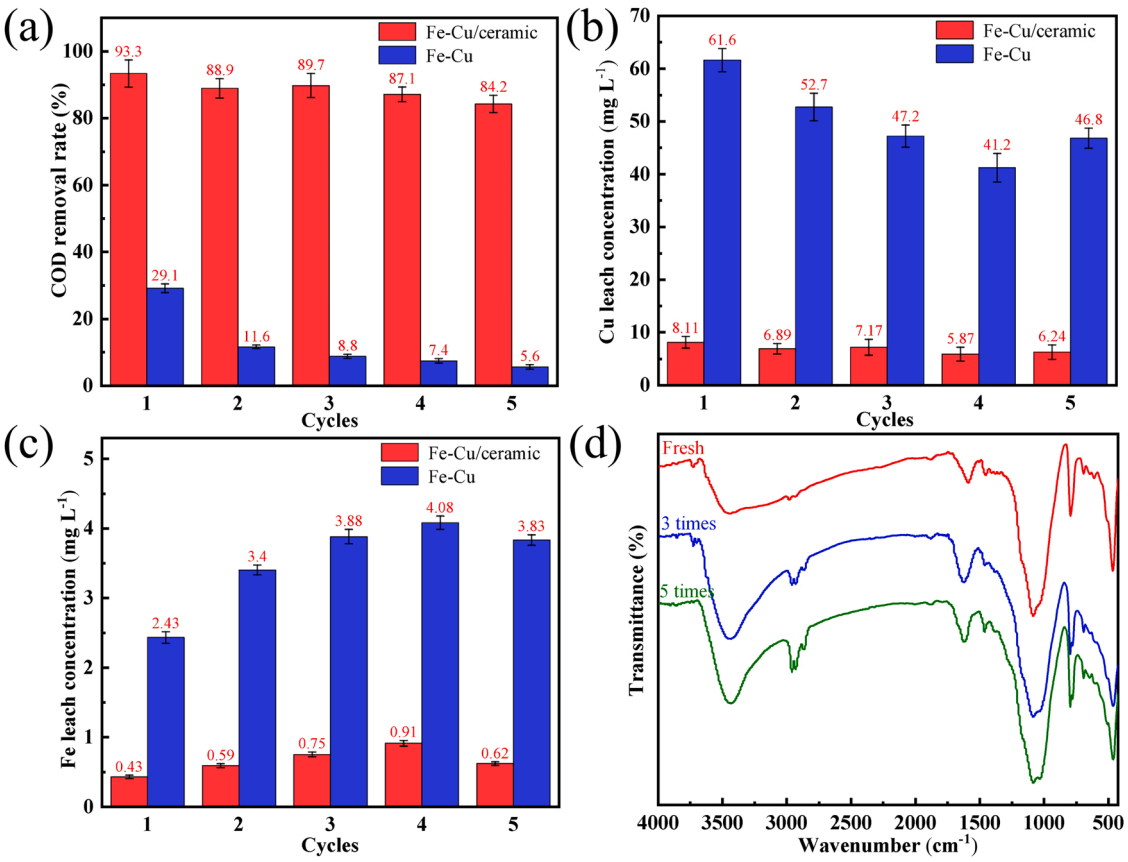

Fig. 7. (a) COD removal, (b) Cu leaching concentration, and (c) Fe leaching concentration in each cycle with Fe–Cu/ceramic and bare Fe–Cu as catalysts; (d) FTIR spectra of the Fe–Cu/ceramic before and after reaction.

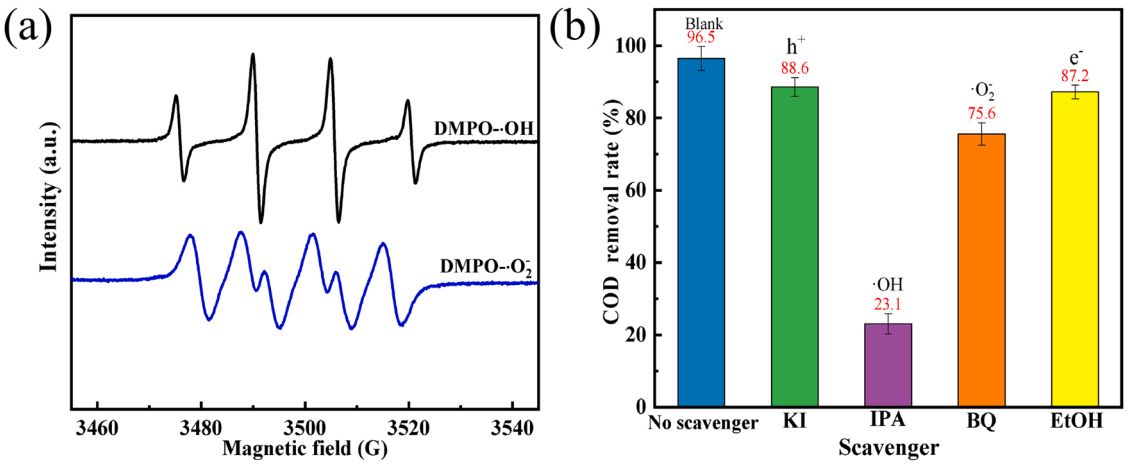

Fig. 8. (a) ESR spectra of DMPO-·OH and DMPO-·O_2^- in Fe–Cu/ceramic + H_2O_2 + Vis system; (b) effects of radical scavengers on COD removal rate.

erosion. As the standard reduction potential of Cu^{2+}/Cu^{+} (0.17 V) is much lower than that of Fe^{3+}/Fe^{2+} (0.77 V) [26], it could be proved that Fe^{3+} was reduced by Cu^{+}, which further explains the increased contents of Cu^{2+} and Fe^{2+}. In addition, the peak area ratio of O 1s peak at 533.3 eV decreased from 17.2% to 6.5% (Fig. 9b), indicating that the surface hydroxylation of Fe–Cu/ceramic promoted the generation of·OH to improve the catalytic efficiency of photo-Fenton reaction.

Based on the above results, a possible photo-Fenton catalytic mechanism for the degradation of the wastewater over Fe–Cu/ceramic is proposed and shown in Fig. 10. It is mainly comprised of following steps: (1) under visible-light irradiation, the Fe–Cu/ceramic catalyst was excited to produce e^{-}/h^{+} pair pairs (Eq. (3)); (2) the e^{-} rapidly migrated to the surface of the catalyst by the action of electric field, and the Fe^{3+} and Cu^{2+} were quickly reduced to Fe^{2+} and Cu^{+} (Eqs. (4) and (5)), which combined with dissolved oxygen in water to form·O_2^- (Eq. 6); (3) Cu^0 could serve as electron donor to reduce Fe^{3+} to Fe^{2+} (Eq. (7)) and be eroded to form Cu^{+}. The increase of Cu^{+} was conducive to the rapid and stable transformation of Fe^{3+} to Fe^{2+}, thus increasing the concentration of Fe^{2+} (Eqs. (8) and (9)) and generating more·OH radicals; (4) Fe^{3+}/Fe^{2+} and Cu^{2+}/Cu^{+} showed self-cycling in the degradation process (Eqs. (10)–(14)), which could keep the stability of the photo-Fenton reaction. Finally,·OH and·O_2^- free radicals degraded the target pollutant to small

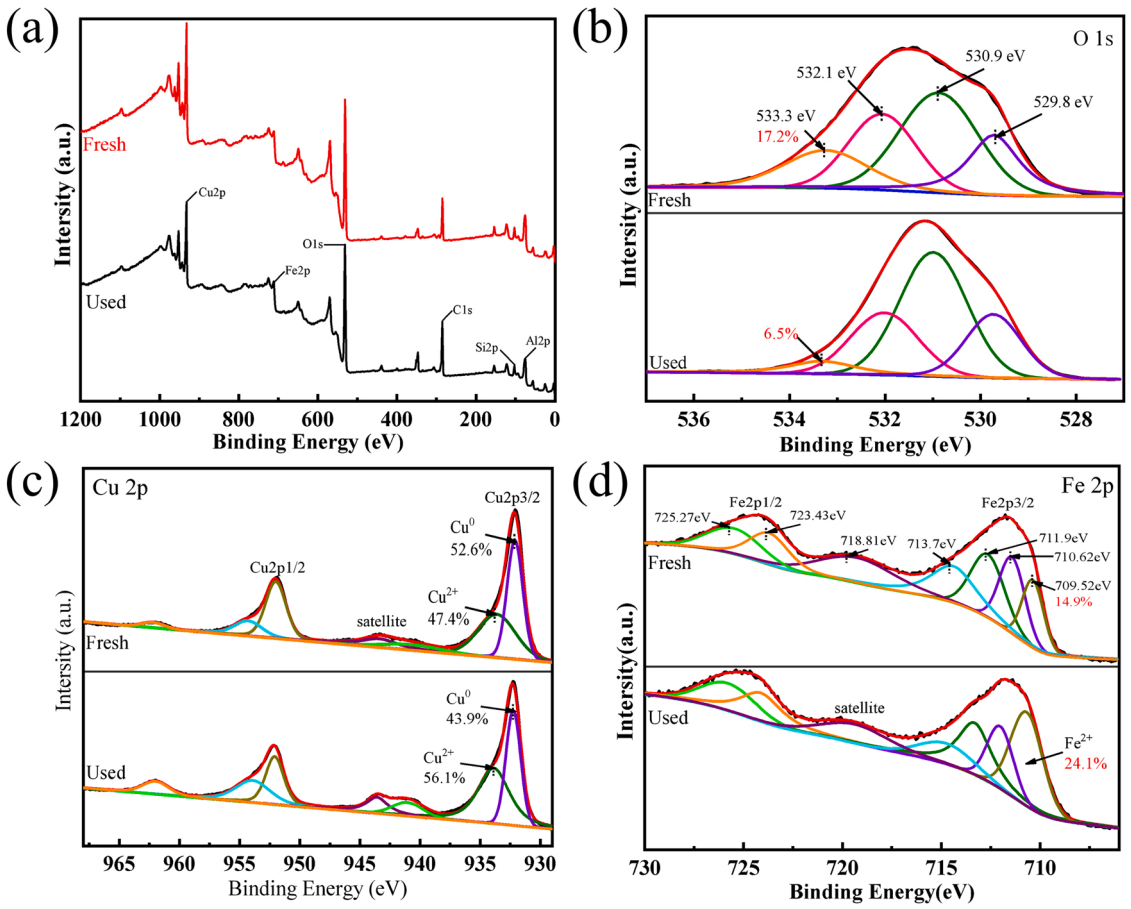

Fig. 9. XPS spectra of (a) survey, (b) O 1 s, (c) Cu 2p, and (d) Fe 2p of the Fe–Cu/ceramic before and after photo-Fenton reaction.

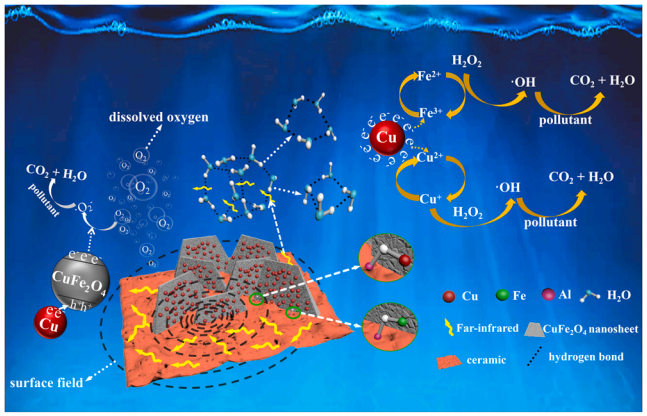

Fig. 10. Schematic illustration of photo-Fenton reaction catalyzed by Fe–Cu/ceramic.

molecules, which could be further degraded into CO_2 and H_2O (Eq. (15)). Compared with other catalysts, Fe–Cu/ceramic composite showed excellent catalytic activity, ascribed to that the ceramic was beneficial for uniform dispersion of the Fe–Cu components to increase the reactive sites, and the special structure promoted the light absorption. The surface electric field and far-infrared properties of the ceramic accelerated the separation of e^-/h^+ pairs and inhibited their recombination, reduced the size of water clusters, and increased dissolved oxygen, thus promoting the generation of $\cdot O_2^-$.

$$\text{Fe–Cu/ceramic} + hv \rightarrow e^- + h^+ \quad (3)$$

$$\equiv Fe^{3+} + e^- \rightarrow Fe^{2+} \quad (4)$$

$$\equiv Cu^{2+} + e^- \rightarrow \equiv Cu^{+} \quad (5)$$

$$O_2 + e^- \rightarrow \cdot O_2^- \quad (6)$$

$$Cu^0 + \equiv Fe^{3+} \rightarrow \equiv Fe^{2+} + \equiv Cu^{2+} \quad (7)$$

$$Cu^0 + H_2O_2 + H+ \rightarrow \equiv Cu^{+} + H_2O \quad (8)$$

$$\equiv Cu^{+} + \equiv Fe^{3+} \rightarrow \equiv Cu^{2+} + \equiv Fe^{2+} \quad (9)$$

$$\equiv Fe^{3+} + H_2O_2 \rightarrow \equiv Fe^{2+} + \cdot OOH + H^+ \quad (10)$$

$$\equiv Fe^{2+} + H_2O_2 \rightarrow \equiv Fe^{3+} + \cdot OH + OH^- \quad (11)$$

$$\equiv Cu^{+} + H_2O_2 \rightarrow \equiv Cu^{2+} + \cdot OH + OH^- \quad (12)$$

$$\equiv Cu^{2+} + H_2O_2 \rightarrow \equiv Cu^{+} + \cdot OOH + H^+ \quad (13)$$

$$\cdot OOH \leftrightarrow \cdot O_2^- + H^+ \quad (14)$$

$$\cdot OH + \cdot O_2^- + \text{pollutant} \rightarrow CO_2 + H_2O \quad (15)$$

4. Conclusion

In summary, the Fe–Cu/ceramic composites with surface electric field and far-infrared properties were successfully synthesized and applied for photo-Fenton catalytic degradation of the wastewater generated from H_2O_2 production. The Fe–Cu/ceramic composite with the mass ratio of 1:2:2 ($CuFe_2O_4$:copper acetate:ceramic) presented the highest catalytic activity. Under the optimized conditions, the highest

COD removal rate of the wastewater was 98.3%, and the effluent COD was 68.6 mg L^{-1}, which could meet the effluent standard of the Alliance. This might be ascribed to that the introduction of ceramic resulted in high specific surface area and pore volume of the Fe–Cu/ceramic, thus providing more reactive sites. Moreover, the surface electric field and far-infrared ray of the ceramic enhanced the visible-light absorption of Fe–Cu/ceramic, and shortened the reaction path of photo-Fenton induced electron to generate free radicals. The Fe–Cu/ceramic exhibited great reusability due to the stable loading of Fe–Cu nanoparticles on ceramic with Fe–O–Al and Cu–O–Al bonds, which reduced the leaching of metal ions. The ESR and quenching experimental results showed that the·OH and·O_2^- were the main active species in Fe–Cu/ceramic + H_2O_2 + Vis reaction system. The·OH free radicals were generated by Fe^{3+}/Fe^{2+} and Cu^{2+}/Cu^{+} cycles, while the·O_2^- radicals were mainly formed by dissolved oxygen capturing e^-. This work would provide a new idea for effective catalytic degradation of the wastewater by using natural mineral-based composites as photo-Fenton catalyst.

CRediT authorship contribution statement

Zongxian Hong: Conceptualization, Methodology, Software, Validation, Writing – original draft. **Xiunan Cai:** Conceptualization, Data curation, Investigation. **Wuxiang Zhang:** Validation, Methodology, Validation. **Songlin Fan**: Data curation, Methodology, Investigation. **Yanjuan Zhang:** Conceptualization, Funding acquisition, Methodology, Supervision, Project administration, Writing – review & editing. **Tao Gan**: Visualization, Investigation. **Huayu Hu:** Supervision, Resources. **Zuqiang Huang**: Conceptualization, Funding acquisition, Methodology, Supervision, Writing – review & editing.

Declaration of Competing Interest

The authors declare that they have no known competing financial interests or personal relationships that could have appeared to influence the work reported in this paper.

Acknowledgments

This research was supported by National Natural Science Foundation of China (Nos. 22068007 and 22008041) and Guangxi Natural Science Foundation, China (Nos. 2019GXNSFDA245020 and 2020GXNSFGA297001).

Appendix A. Supporting information

Supplementary data associated with this article can be found in the online version at doi:10.1016/j.jece.2022.107687.

References

[1] M. Ali, U. Farooq, S. Lyu, Y. Sun, M. Li, A. Ahmad, A. Shan, Z. Abbas, Synthesis of controlled release calcium peroxide nanoparticles (CR-nCPs): Characterizations, H_2O_2 liberate performances and pollutant degradation efficiency, Sep Purif. Technol. 241 (2020), 116729.
[2] B.J. Borah, Y. Yamada, P. Bharali, Unravelling the role of metallic Cu in Cu-$CuFe_2O_4$/C nanohybrid for enhanced oxygen reduction electrocatalysis, Acs Appl. Energ. Mater. 3 (2020) 3488–3496.
[3] X. Cai, Q. Huang, Z. Hong, Y. Zhang, H. Hu, Z. Huang, J. Liang, Y. Qin, Cu anchored on manganese residue through mechanical activation to prepare a Fe-Cu@SiO_2/starch-derived carbon composites with highly stable and active visible light photocatalytic performance, J. Environ. Chem. Eng. 9 (2021), 104710.
[4] X. Chen, M. Zhang, H. Qin, J. Zhou, Q. Shen, K. Wang, W. Chen, M. Liu, N. Li, Synergy effect between adsorption and heterogeneous photo-Fenton-like catalysis on $LaFeO_3$/lignin-biochar composites for high efficiency degradation of ofloxacin under visible light, Sep Purif. Technol. 280 (2022), 119751.
[5] L. Cui, Z. Li, Q. Li, M. Chen, W. Jing, X. Gu, Cu/$CuFe_2O_4$ integrated graphite felt as a stable bifunctional cathode for high-performance heterogeneous electro-Fenton oxidation, Chem. Eng. J. 420 (2021), 127666.
[6] X. Dong, B. Ren, Z. Sun, C. Li, X. Zhang, M. Kong, S. Zheng, D.D. Dionysiou, Monodispersed $CuFe_2O_4$ nanoparticles anchored on natural kaolinite as highly efficient peroxymonosulfate catalyst for bisphenol A degradation, Appl. Catal. B-Environ. 253 (2019) 206–217.
[7] Y. Feng, D. Wu, Y. Deng, T. Zhang, K. Shih, Sulfate Radical-Mediated Degradation of Sulfadiazine by $CuFeO_2$ Rhombohedral Crystal-Catalyzed Peroxymonosulfate: Synergistic Effects and Mechanisms, Environ. Sci. Technol. 50 (2016) 3119–3127.
[8] S. Guo, W. Yang, L. You, J. Li, J. Chen, K. Zhou, Simultaneous reduction of Cr(VI) and degradation of tetracycline hydrochloride by a novel iron-modified rectorite composite through heterogeneous photo-Fenton processes, Chem. Eng. J. 393 (2020), 124758.
[9] Y. Guo, C. Dai, Z. Lei, B. Chen, X. Fang, Synthesis of hydrogen peroxide over Pd/SiO_2/COR monolith catalysts by anthraquinone method, Catal. Today 276 (2016) 36–45.
[10] Z. Guo, J. Feng, Y. Feng, D.G. Evans, D. Li, In situ synthesis of solid base catalysts for the regeneration of degradation products formed during the anthraquinone process for the manufacture of hydrogen peroxide, Appl. Catal. A-Gen. 401 (2011) 163–169.
[11] G. Huang, C. Wang, C. Yang, P. Guo, H. Yu, Degradation of Bisphenol A by Peroxymonosulfate Catalytically Activated with $Mn_{1.8}Fe_{1.2}O_4$ Nanospheres: Synergism between Mn and Fe. Environ. Sci. Technol. 51 (2017) 12611–12618.
[12] T. Huang, J. Zhu, S. Ge, T. Guo, C. Jiang, L. Xie, Synthesis of novel CdSe QDs/$BiFeO_3$ composite catalysts and its application for the photo-Fenton catalytic degradation of phenol, J. Environ. Chem. Eng. 8 (2020), 104384.
[13] S. Keerthana, R. Yuvakkumar, G. Ravi, S. Pavithra, M. Thambidurai, C. Dang, D. Velauthapillai, Pure and Ce-doped spinel $CuFe_2O_4$ photocatalysts for efficient rhodamine B degradation, Environ. Res 200 (2021), 111528.
[14] M. Kim, G. Han, X. Xiao, J. Song, J. Hong, E. Jung, H. Kim, J. Ahn, S.S. Han, K. Lee, T. Yu, Anisotropic growth of Pt on Pd nanocube promotes direct synthesis of hydrogen peroxide, Appl. Surf. Sci. 562 (2021), 150031.
[15] H.W. Lee, H. Nam, G. Han, Y. Cho, B.C. Yeo, M. Kim, D. Kim, K. Lee, S.Y. Lee, S. S. Han, Solid-solution alloying of immiscible Pt and Au boosts catalytic performance for H_2O_2 direct synthesis, Acta Mater. 205 (2021), 116563.
[16] C. Li, Z. Sun, W. Zhang, C. Yu, S. Zheng, Highly efficient g-C_3N_4/TiO_2/kaolinite composite with novel three-dimensional structure and enhanced visible light responding ability towards ciprofloxacin and S. aureus, Appl. Catal. B-Environ. 220 (2018) 272–282.
[17] C. Li, N. Zhu, X. Dong, X. Zhang, T. Chen, S. Zheng, Z. Sun, Tuning and controlling photocatalytic performance of TiO_2/kaolinite composite towards ciprofloxacin: Role of 0D/2D structural assembly, Adv. Powder Technol. 31 (2020) 1241–1252.
[18] J. Li, X. Li, J. Han, F. Meng, J. Jiang, J. Li, C. Xu, Y. Li, Mesoporous bimetallic Fe/Co as highly active heterogeneous Fenton catalyst for the degradation of tetracycline hydrochlorides, Sci. Rep. -uk (2019) 9.
[19] Z. Li, C. Guo, J. Lyu, Z. Hu, M. Ge, Tetracycline degradation by persulfate activated with magnetic Cu/$CuFe_2O_4$ composite: Efficiency, stability, mechanism and degradation pathway, J. Hazard Mater. 373 (2019) 85–96.
[20] J. Liu, Z. Jia, W. Zhou, X. Liu, C. Zhang, B. Xu, G. Wu, Self-assembled MoS_2/magnetic ferrite $CuFe_2O_4$ nanocomposite for high-efficiency microwave absorption, Chem. Eng. J. 429 (2022), 132253.
[21] X. Liu, J. Zhou, D. Liu, L. Li, W. Liu, S. Liu, C. Feng, Construction of Z-scheme $CuFe_2O_4$/MnO_2 photocatalyst and activating peroxymonosulfate for phenol degradation: Synergistic effect, degradation pathways, and mechanism, Environ. Res 200 (2021), 111736.
[22] Z. Liu, X. Cai, S. Fan, Y. Zhang, H. Hu, Z. Huang, J. Liang, Y. Qin, Preparation of a stable polyurethane sponge supported Sn-doped ZnO composite via double-template-regulated bionic mineralization for visible-light-driven photocatalytic degradation of tetracycline, J. Environ. Chem. Eng. 9 (2021), 105541.
[23] G. Luo, A. Chen, M. Zhu, K. Zhao, X. Zhang, S. Hu, Improving the electrocatalytic performance of Pd for formic acid electrooxidation by introducing tourmaline, Eectrochim. Acta 360 (2020), 137023.
[24] S. Ma, J. Jing, P. Liu, Z. Li, W. Jin, B. Xie, Y. Zhao, High selectivity and effectiveness for removal of tetracycline and its related drug resistance in food wastewater through schwertmannite/graphene oxide catalyzed photo-Fenton-like oxidation, J. Hazard Mater. 392 (2020), 122437.
[25] X. Ma, R. Hao, Z. Wang, P. Xu, Y. Luo, Y. Zhao, Nanoscale $CuFe_2O_4$ monodispersedly anchored on reduced graphene oxide as excellent peroxydisulfate catalyst for removal of gaseous elemental mercury, Chem. Eng. J. 401 (2020), 126101.
[26] H. Mohamed, E. Chikoidze, A. Ratep, A.M.A. Elsoud, M. Boshta, M.B.S. Osman, Synthesis of conducting single-phase $CuFeO_2$ thin films by spray pyrolysis technique, Mat. Sci. Semicon Proc. 107 (2020), 104831.
[27] S. Pal, S. Kumar, A. Verma, A. Kumar, T. Ludwig, M. Frank, S. Mathur, R. Prakash, I. Sinha, Development of magnetically recyclable visible light photocatalysts for hydrogen peroxide production, Mat. Sci. Semicon Proc. 112 (2020), 105024.
[28] Z. Qu, Y. Muhammad, W. He, J. Li, Z. Gao, J. Fu, S. Jalil Shah, H. Sun, J. Wang, Z. Huang, Z. Zhao, Designing C-Fe-O bonded MIL-88B(Fe)/jasmine petal-derived-carbon composite biosensor for the simultaneous detection of dopamine and uric acid, Chem. Eng. J. 404 (2021), 126570.
[29] J. Tzeng, C. Weng, Y. Lin, S. Huang, L. Yen, J. Anotai, Y. Lin, Synthesis, characterization, and visible light induced photoactivity of tourmaline-N-TiO_2 composite for photooxidation of ethylene, J. Ind. Eng. Chem. 80 (2019) 376–384.
[30] C. Wang, Q. Chen, T. Guo, Q. Li, Environmental effects and enhancement mechanism of graphene/tourmaline composites, J. Clean. Prod. 262 (2020), 121313.
[31] F. Wang, C. Wang, X. Du, Y. Li, F. Wang, P. Wang, Efficient removal of emerging organic contaminants via photo-Fenton process over micron-sized Fe-MOF sheet, Chem. Eng. J. 429 (2022), 132495.

[32] L. Wang, Y. Zhang, J. Qian, Graph. aerogel-Based Catal. Fenton- React. Water Decontam.: a Short. Rev. 8 (2021), 100171.
[33] L. Xu, L. Zhao, Y. Mao, Z. Zhou, D. Wu, Enhancing the degradation of bisphenol A by dioxygen activation using bimetallic Cu/Fe@zeolite: Critical role of Cu(I) and superoxide radical, Sep Purif. Technol. 253 (2020), 117550.
[34] Y. Xu, J. Ai, H. Zhang, The mechanism of degradation of bisphenol A using the magnetically separable $CuFe_2O_4$/peroxymonosulfate heterogeneous oxidation process, J. Hazard Mater. 309 (2016) 87–96.
[35] Y. Yan, X. Ou, H. Zhang, 17O NMR and Raman spectra of water with different calcium salts, J. Mol. Struct. 1074 (2014) 310–314.
[36] P. Ye, D. Wu, M. Wang, Y. Wei, A. Xu, X. Li, Coating magnetic $CuFe_2O_4$ nanoparticles with OMS-2 for enhanced degradation of organic pollutants via peroxymonosulfate activation, Appl. Surf. Sci. 428 (2018) 131–139.
[37] C. Yu, Z. Tong, S. Li, Y. Yin, Enhancing the photocatalytic activity of ZnO by using tourmaline, Mater. Lett. 240 (2019) 161–164.
[38] L. Yu, C. Wang, F. Chen, J. Zhang, Y. Ruan, J. Xu, Investigating the synergistic effects in tourmaline/TiO_2-based heterogeneous photocatalysis: Underlying mechanism insights, J. Mol. Catal. A-Chem. 411 (2016) 1–8.
[39] Z. Yu, H. Li, X. Liu, C. Xu, H. Xiong, Influence of soil electric field on water movement in soil, Soil Res 155 (2016) 263–270.
[40] W. Yuan, J. Kuang, M. Yu, Z. Huang, Z. Zou, L. Zhu, Facile preparation of MoS_2@ Kaolin composite by one-step hydrothermal method for efficient removal of Pb(II), J. Hazard Mater. 405 (2021), 124261.
[41] B. Zhang, Y. Hou, Z. Yu, Y. Liu, J. Huang, L. Qian, J. Xiong, Three-dimensional electro-Fenton degradation of Rhodamine B with efficient Fe-Cu/kaolin particle electrodes: Electrodes optimization, kinetics, influencing factors and mechanism, Sep Purif. Technol. 210 (2019) 60–68.
[42] H. Zhang, Y. Song, L. Nengzi, J. Gou, B. Li, X. Cheng, Activation of persulfate by a novel magnetic $CuFe_2O_4/Bi_2O_3$ composite for lomefloxacin degradation, Chem. Eng. J. 379 (2020), 122362.
[43] X. Zhang, B. Ren, X. Li, B. Liu, S. Wang, P. Yu, Y. Xu, G. Jiang, High-efficiency removal of tetracycline by carbon-bridge-doped g-C_3N_4/Fe_3O_4 magnetic heterogeneous catalyst through photo-Fenton process, J. Hazard Mater. 418 (2021), 126333.
[44] C. Zhao, D. Huang, J. Chen, DFT study for combined influence of C-doping and external electric field on electronic structure and optical properties of TiO_2 (001) surface, J. Mater. 4 (2018) 247–255.
[45] S. Zhao, T. Guo, X. Li, T. Xu, B. Yang, X. Zhao, Carbon nanotubes covalent combined with graphitic carbon nitride for photocatalytic hydrogen peroxide production under visible light, Appl. Catal. B-Environ. 224 (2018) 725–732.
[46] W. Zhao, Y. Jin, C.H. Gao, W. Gu, Z.M. Jin, Y.L. Lei, L.S. Liao, A simple method for fabricating p–n junction photocatalyst $CuFe_2O_4/Bi_4Ti_3O_{12}$ and its photocatalytic activity, Mater. Chem. Phys. 143 (2014) 952–962.
[47] Z. Zhao, X. Cai, S. Fan, Y. Zhang, Z. Huang, H. Hu, J. Liang, Y. Qin, Construction of a stable Cu-Fe@C composite catalyst with enhanced performance and recyclability for visible-light-driven photo-Fenton reaction, J. Alloy Compd. 877 (2021), 160260.